International Journal of Heat and Mass Transfer 55 (2012) 2953–2964

Contents lists available at SciVerse ScienceDirect

International Journal of Heat and Mass Transfer

journal homepage: www.elsevier.com/locate/ijhmt

Methodology for predicting spray quenching of thick-walled metal alloy tubes

Nikhin Mascarenhas, Issam Mudawar *

Boiling and Two-Phase Flow Laboratory, School of Mechanical Engineering, Purdue University, West Lafayette, IN 47907, USA

ARTICLE INFO

Article history:
Received 17 August 2011
Received in revised form 3 February 2012
Accepted 3 February 2012
Available online 22 March 2012

Keywords:
Spray cooling
Quenching
Boiling curve

ABSTRACT

This paper explores the parametric influences of spray quenching for thick-walled metal alloy tubes. Using the point-source depiction of a spray, an analytical model is derived to determine the shape and size of the spray impact zone, as well as the distribution of volumetric flux across the same zone. This distribution is incorporated into heat transfer correlations for all spray boiling regimes to generate a complete boiling curve for every location across the impact zone. By setting boundary conditions for both the sprayed and unsprayed portions of the tube surface, a heat diffusion model is constructed for a unit cell of the tube for both aluminum alloy and steel. This model is used to construct spray quench curves for every point along the sprayed surface and within the wall. Increasing nozzle pressure drop or decreasing orifice-to-surface distance are shown to increase the magnitude of volumetric flux, which hastens the onset of the rapid cooling stages of the quench as well as improves overall cooling effectiveness. The sprayed surface is characterized by fast thermal response to the spray, while regions within the wall display more gradual response due to heat diffusion delays. With their superior thermal diffusivity, aluminum alloy tubes transmit the cooling effect through the wall faster than steel tubes. For steel, the cooling effect is more concentrated near the sprayed surface, causing the sprayed surface to cool much faster and locations within the wall much slower than for aluminum alloy. The predictive approach presented in this paper facilitates the determination of surface temperature gradients in the quenched part to guard against stress concentration. Also, when combined with metallurgical transformation models for the alloy, it may be possible to predict material properties such as hardness and strength.

1. Introduction

Intense heat dissipation from surfaces is a common concern in many industries. High-flux cooling solutions include pool boiling [1,2], parallel forced convection boiling [3,4], jet impingement [5,6] and spray cooling. Also, both coolant additives [7] and surface augmentation techniques [8–10] are commonly used to enhance the rate of heat removal. The present study concerns the use of sprays to cool un-augmented surfaces.

Tubes constitute a common shape that is found in a high percentage of processed alloy components. They are used in a variety of applications that include hydraulic cylinders, pivot pin chambers, gun barrels and plumbing conduits. These applications place primary emphasis on the strength, hardness and scratch resistance of their constituent alloy tubes. It is therefore of vital importance to subject these tubes to a controlled heat treatment process that ensures optimal mechanical properties. While bath quenching is commonly used in most heat treatment operations, absence of spatial control of the cooling process in a bath often results in a myriad of local imperfections such as distortion, soft spots and regions of poor hardness and poor strength. These problems can be alleviated by the use of sprays in the quenching stage of heat treatment.

A spray consists of a multitude of droplets with controlled sizes, speeds and trajectories, and is popular in many cooling applications [11]. Two primary cooling advantages of sprays compared to competing cooling schemes are their ability to increase heat transfer effectiveness and spread the cooling over a broad surface area. Their heat transfer effectiveness is a result of the large liquid surface area-to-volume ratio achieved by liquid breakup into fine droplets.

The present study concerns the use of plain-orifice sprays that achieve the liquid breakup by forcing the incoming liquid flow through a small orifice. Breakup can also be achieved with the aid of a tangential air stream in so-called air-assist sprays, which are beyond the scope of the present study.

The complex interaction between the spray and hot alloy surface can be understood by breaking it down into its dominant process variables, namely, the hydrodynamic structure of the spray itself, the placement of the spray nozzle relative to the surface, and the geometry and heat diffusion characteristics of the alloy itself. The spray parameters that have the strongest influence on cooling performance are volumetric flux, Q'', Sauter mean

* Corresponding author. Tel.: +1 765 494 5705; fax: +1 765 494 0539.
E-mail address: mudawar@ecn.purdue.edu (I. Mudawar).
URL: https://engineering.purdue.edu/BTPFL (I. Mudawar).

0017-9310/$ - see front matter © 2012 Elsevier Ltd. All rights reserved.
doi:10.1016/j.ijheatmasstransfer.2012.02.018

Nomenclature

a	half-length of major diameter of elliptical impact area
A	area formed by projecting spherical surface A' on inner surface of tube
A'	area of spherical surface bound by spray's cone angle and centered at spray orifice, and whose radius is equal to distance from orifice to inner surface of tube
b	half-length of minor diameter of elliptical impact area
CHF	critical heat flux
c_p	specific heat at constant pressure
D	inside diameter of tube
d_o	diameter of nozzle's orifice
d_{32}	Sauter mean diameter
h	heat transfer coefficient
H	distance from orifice to inner surface of tube
h_{fg}	latent heat of vaporization
k	thermal conductivity
K	nozzle's flow coefficient
$Nu_{d_{32}}$	Nusselt number based on d_{32}; hd_{32}/k_f
ΔP	pressure drop across spray nozzle
Pr	Prandtl number
Q	total volumetric flow rate of spray
Q''	local volumetric flux across sprayed surface
Q''_{sp}	uniform volumetric flux along spherical surface bound by spray's cone angle and centered at spray nozzle's orifice, and whose radius is equal to distance form orifice to inner surface of tube
q''	heat flux
$q''_{m,p}$	local (point-based) critical heat flux
r	coordinate defined in Fig. 3
Re_{d_o}	Reynolds number based on nozzle's orifice diameter
Red_{32}	Reynolds number based on d_{32}; $\rho_f Q'' d_{32}/\mu_f$
T	temperature
T_f	spray liquid temperature
T_s	surface temperature
T_{sat}	saturation temperature
ΔT	difference between surface and liquid temperatures, $T_s - T_f$
ΔT_{sub}	subcooling of spray liquid, $T_{sat} - T_f$
u_m	mean droplet velocity
We_{d_o}	Weber number based on nozzle's orifice diameter
x	coordinate defined in Fig. 3
z	coordinate defined in Fig. 3

Greek Symbols

β	angle defined in Fig. 4
γ	angle defined in Fig. 4
θ	cone angle of spray
μ	viscosity
ρ	density
σ	surface tension
φ	half-angle defined in Fig. 4

Subscripts

a	ambient air
CHF	critical heat flux
DFB	departure from film boiling
f	liquid
g	vapor
MIN	minimum heat flux (Leidenfrost point)
OSP	onset of single-phase liquid cooling
s	tube's surface
sat	saturation
sub	subcooling

diameter, d_{32}, and mean drop velocity, u_m [12–24]. Volumetric flux is the ratio of volume flow rate of coolant impacting an infinitesimal portion of the surface to the area of the same portion; hence it has the units of velocity. This parameter is influenced by the spray nozzle's orifice-to-surface distance as well as distance from the spray axis. The Sauter mean diameter is defined as the diameter of a drop having the same volume-to-surface area ratio as the entire spray.

For a plain-orifice spray, droplet breakup does not occur at the nozzle exit, but requires a finite distance downstream of the nozzle, and the orifice-to-surface distance is always maintained greater than this distance to ensure reliable and predictable cooling behavior. Downstream from the droplet breakup region, both d_{32} and u_m are fairly constant both along the spray axis and away from the axis for orifice-to-surface distances of practical interest. However, Q'' decreases monotonically both along and away from the spray axis. Because of the strong dependence of spray cooling effectiveness on Q'', these spatial variations must be taken into account when configuring a spray quenching system. The bounds of the spray impact area as well as the spatial variations of volumetric flux on a flat surface have been well established, both in terms of measured distributions and analytical formulation [20,21].

1.1. Boiling curve and quench curve

The heat transfer response of the hot impact surface is described by both the boiling curve and the quench curve; the relationship between the two curves is described here for the simple case of bath quenching. Shown in Fig. 1(a), the boiling curve depicts the variation of heat flux from the surface to the spray with surface temperature. It is highly effective at identifying the different heat transfer regimes that the surface traverses as it is cooled from a very high initial temperature. Cooling is initiated in the *film-boiling regime*, where a thin vapor layer quickly encases the surface, preventing any liquid contact with the surface, which explains the poor heat transfer effectiveness of this regime. The vapor layer begins to collapse at the *minimum heat flux point*, commonly referred to as the *Leidenfrost point*. Further decrease in surface temperature facilitates intermittent liquid contact with the surface and improved cooling in the *transition boiling regime*. The heat flux from the surface reaches a maximum at the c *ritical heat flux (CHF) point*, where the vapor layer breaks down entirely. Beyond this point, cooling rate is greatly improved in the *nucleate boiling regime* as the entire surface becomes available for liquid contact and ensuing vapor production. Quenching is terminated in the slow *single-phase liquid cooling regime* after all boiling activity subsides. An important observation from the boiling curve is that the Leidenfrost point marks a transition point between slow and fast cooling rates; this point therefore has a strong bearing on the overall effectiveness of the quench.

The quench curve shown in Fig. 1(b) is a better representation of cooling rate than the boiling curve. Unlike the boiling curve, which is a measure of surface effects, the quench curve also accounts for the thermal mass of the quenched part. The afore-mentioned boiling regimes are associated with significant slope changes along the quench curve, starting with slow cooling in the film boiling regime down to the Leidenfrost point, beyond which cooling rate increases in the transition boiling regime, and more appreciably in the nucleate boiling regime, before subsiding in the single-phase liquid cooling regime. This curve again

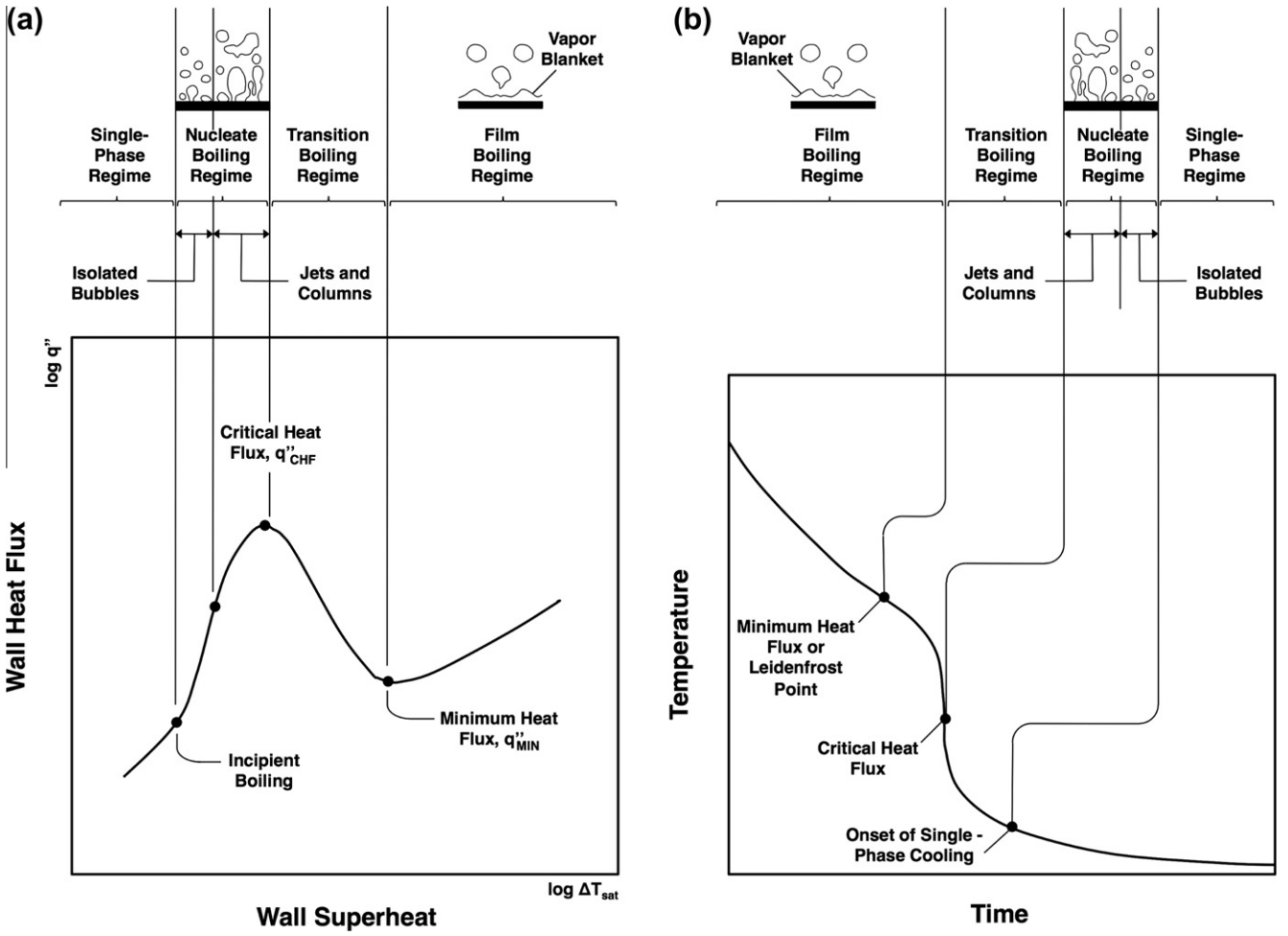

Fig. 1. (a) Boiling curve and (b) corresponding quench curve.

emphasizes the importance of predicting the onset of the Leidenfrost point as a transition point between the slow and fast cooling phases of the quench. Aside from the Leidenfrost point, predictive tools are required for each boiling regime to enable accurate determination of the temperature response of the quenched part to the spray. Those tools must be presented in terms of known spray parameters [13–24].

1.2. Heat treatment and quenching requirements

Configuring an effective spray quenching system for heat treatment of alloys is strongly dependent on understanding (1) the spray-surface interactions, (2) the thermal response of the quenched part, and (3) the ensuing metallurgical transformations in the part following the heat treatment. The heat treatment process consists of three stages: *solution heat treating, quenching* and *age hardening*. Solution heat treating involves heating the alloy close to the liquidus temperature to allow the alloying elements to diffuse into the primary metal grain structure. This is followed by rapid quenching of the part to temporarily suppress solute precipitation. Age hardening is then achieved by reheating the part to a temperature below the solvus for a prescribed alloy-dependent period, causing fine dispersion of the precipitates within the primary metal grain structure. These fine precipitates act as dislocation barriers and impart the desired alloy hardness and strength.

Spray quenching has two significant advantages over the more conventional bath quenching. First, sprays provide higher cooling rates and are therefore better capable at suppressing the aforementioned precipitation of solutes. Additionally, absent any spatial control of the cooling process in bath quenching, parts with irregular cross-sections and large variations in thermal mass are prone to severe distortion due to thermal stresses. This problem can be overcome by replacing the bath with an array of sprays that are optimally positioned relative to the part's surface. Here, thicker sections are subjected to denser sprays and thinner sections to lighter sprays such that the entire part cools at a fast but fairly uniform rate. For a spray quenching system utilizing identical spray nozzles, local cooling rate can be manipulated by changing supply pressure or orifice-to-surface distance or both.

1.3. Spray cooling of curved surfaces

Most published spray cooling studies involve flat surfaces and the literature concerning cooling of curved surfaces is quite sparse. Hodgson et al. [25] examined the cooling of a brass cylinder by a water–air spray and found the cooling rate to increase with increasing flow rate of water in the spray. Buckingham and Haji-Sheikh [26] subjected the outer surface of a 316 stainless steel cylinder initially at 1000 °C to a single water–air spray. Better cooling was achieved along the portion of surface normal to the spray axis and directly impacted by the spray. Like Hodgson et al., they were able to improve cooling effectiveness by increasing the flow rate of water in the spray. Albright [27] devised a controlled environment wind tunnel experiment in which the curved surface of a 5.08 cm

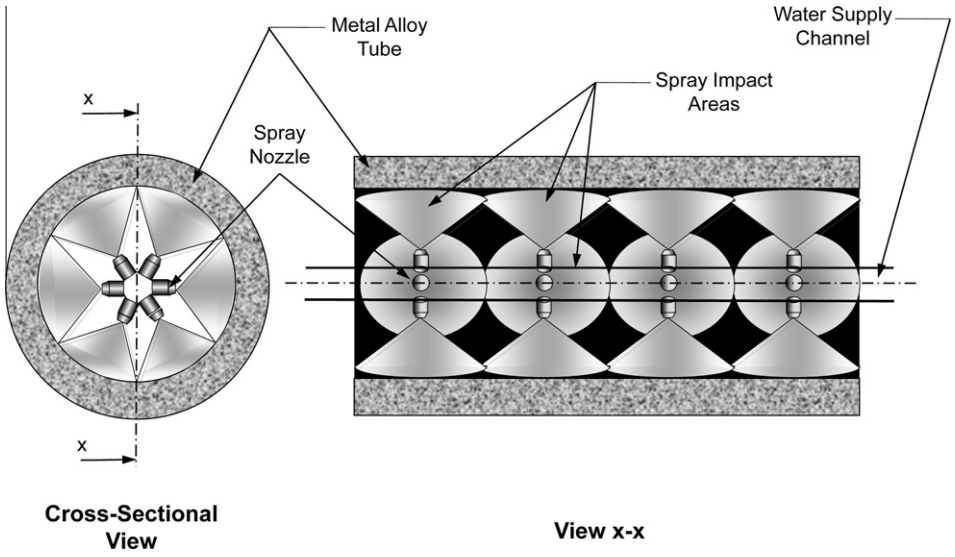

Fig. 2. Spray nozzle configuration for quenching of metal alloy thick-walled tube.

diameter mild steel solid cylinder at 95 °C was exposed to a water–air spray. Heat transfer rate increased substantially by increasing the spray flow rate as well as by optimal orientation of the cylinder's surface relative to the spray. Albright also concluded that spray cooling is substantially more efficient than bath cooling, both in terms of cooling rate and mass flow rate of water used. Other studies also dealt with spray cooling of rods and exteriors of tube bundles [28–33]; however, the sprays used were composed of relatively unsaturated air to simulate de-humidification effects in HVAC systems.

Recently, the authors of the present study presented a methodology for predicting the temperature response of solid alloy cylinders to external cooling by an array of plain-orifice sprays [34]. To tackle spray impact with the outer curved surface of the cylinders, earlier models for volumetric flux distribution were modified and combined with correlations for the different boiling regimes to predict thermal response for different spray conditions.

1.4. Objectives of study

The present study is a follow-up to the study just mentioned, and aims to provide a comprehensive predictive methodology for internal spray quenching of thick-walled metal alloy tubes. Examined in this study are the influences of practical spray parameters (supply pressure and orifice-to-surface distance) and thermal properties of the alloy itself on the temperature response during the spray quench. These influences are used to infer important practical findings concerning thermal stress development as well as the ability to attain superior hardness and strength compared to bath quenching.

2. Spray cooling system and representative section

Fig. 2 shows a spray nozzle arrangement along the axis of a cylindrical thick-walled tube. Water is fed through an axial supply channel that is fitted with radially oriented spray nozzles. The supply channel and nozzles are fully retractable. They are inserted initially along the axis after the heated part is removed from the furnace to initiate the quench, and retracted upon completion of the quench. To maximize spray impact area and ensure both effective and predictable spray distribution, the nozzles are positioned such that the spray impact zones along the inner curved surface of the tube are tangent to one another with no spacing or overlap.

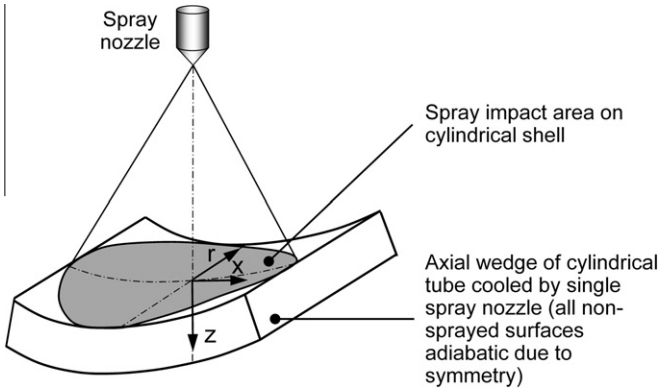

Fig. 3. Spray impact area and shell element modeled in present study. Actual computational domain (unit cell) is one quarter of shell element shown.

Table 1
Characteristics of spray nozzle utilized in present study. P_a = 1 atm, ρ_a = 1.2 kg/m^3, T_f = 100 °C, ρ_f = 957 kg/m^3, σ = 0.0589 N/m, $c_{p,f}$ = 4.217 kK/kg.K, μ_f = 0.00028 Ns/m^2, ρ_g = 0.596 kg/m^3, h_{fg} = 2257 kJ/kg T_f = 23 °C, ρ_f = 998 kg/m^3, μ_f = 0.00091 Ns/m^2, Pr_f = 6.225.

Spray angle θ (°)		45
Nozzle orifice diameter d_o(m)		0.0028
Nozzle coefficient $K \times 10^{-13}$(kg/m^3)		1.7
Total flow rate $Q \times 10^6$ (m^3/s.m^2)	ΔP = 552 kPa	180
	ΔP = 276 kPa	127
	ΔP = 138 kPa	90
Area averaged mean diameter $d_{32} \times 10^6$(m)	ΔP = 552 kPa	89.5
	ΔP = 276 kPa	117
	ΔP = 138 kPa	153
Mean drop velocity u_m (m/s)	ΔP = 552 kPa	20.5
	ΔP = 276 kPa	15.3
	ΔP = 138 kPa	12.1

This arrangement limits the nozzle-to-surface distance to less than the radius of the tube.

A representative portion of the tube is chosen for analysis of the entire tube and quenching system. Shown in Fig. 3, this portion consists of an axial wedge of the tube with its inner surface inscribing a single spray impact area. As discussed later and due to symmetry, a 'unit cell' that will be used for numerical analysis consists of only one-fourth this representative portion. The representative

Table 2
Properties of aluminum and steel.

Density (kg/m^3)	Al-2024 [16]		ASTM A322 [35]	
	2770		7872	
Thermal conductivity (W/m.K)	T = 293 K	178	T = 373 K	44.6
	T = 366 K	185	T = 473 K	43.4
	T = 477 K	190	T = 673 K	37.7
	T = 589 K	187	T = 873 K	31.3
	T = 700 K	173		
Specific heat (J/kg.K)	T = 293 K	850	T = 373 K	452
	T = 366 K	908	T = 473 K	473
	T = 477 K	967	T = 673 K	519
	T = 589 K	1026	T = 873 K	561
	T = 700 K	1130		

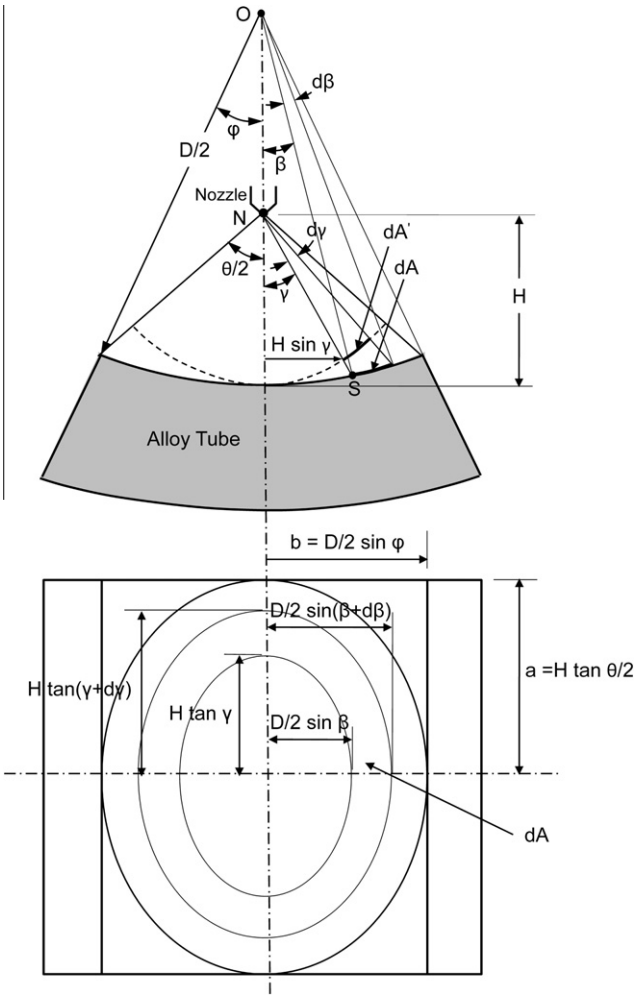

Fig. 4. Spray model.

portion of the tube is subjected to spray cooling along its inner curved surface, while its four radial surfaces are assumed perfectly insulated due to symmetry. Negligible natural convection occurs on the outer curved surface as well as outside the spray impact area of the inner surface; both these regions are assumed perfectly insulated in the present model.

The inner and outer diameters of the unit cell have been set at 0.5 and 0.8 m, respectively. The 0.15 m wall thickness provides adequate radial heat diffusion distance for analysis of the tube's thermal response to the spray quench. Full-cone spray nozzles having a 45° spray angle are considered, while the nozzle pressure drop, ΔP, and orifice-to-surface distance, H, are allowed to vary. Materials considered for analysis are aluminum 2024 and steel (ASTM A322). The spray fluid is pure water, which is supplied at T_f = 23 °C, and the unit cell is assumed initially at a uniform temperature of 427 °C. The characteristics of the water spray nozzles (at 23 and 100 °C) and properties of the two alloys are given in Tables 1 and 2, respectively.

3. Volumetric flux distribution model for inner tube surface

Determination of the spatial distribution of volumetric flux over the inner surface of the tube is a crucial prerequisite for the thermal analysis. Mudawar and Estes [21] analytically determined the volumetric flux distribution over a flat surface, where the spray impact area (spray zone) is circular. They assumed a uniform distribution of the total spray flow rate, Q, over any spherical surface centered at the spray orifice and bound by the spray cone angle, θ.

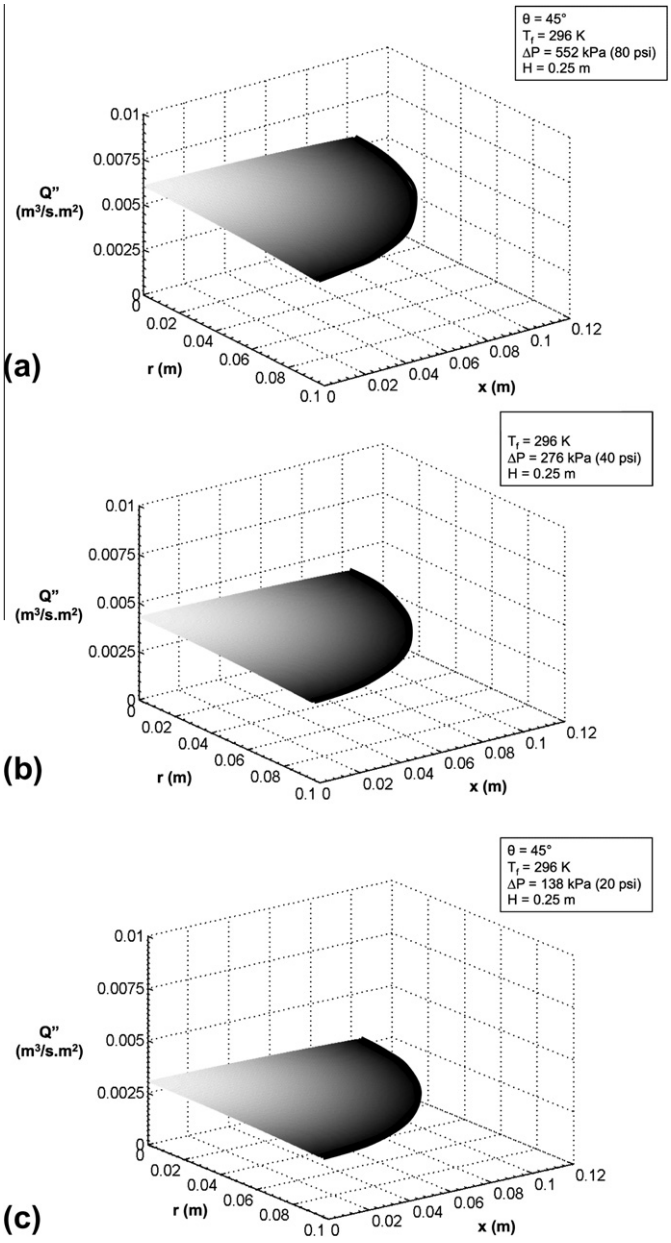

Fig. 5. Volumetric flux distributions for H = 0.25 m with (a) ΔP = 552 kPa (80 psi), (b) ΔP = 276 kPa (40 psi), and (c) ΔP = 138 kPa (20 psi).

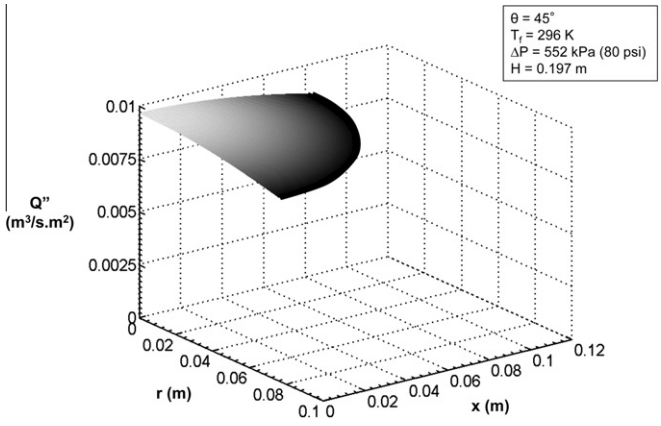

Fig. 6. Volumetric flux distribution for $H = 0.197$ m with $\Delta P = 552$ kPa (80 psi).

For the inner curved wall of the representative section, Fig. 3 shows that the projection of the spray zone onto any flat surface normal to the spray axis is elliptic. This is a consequence of the shorter distance that the spray has to travel before impacting the curved surface, which reduces the spray zone axis along the curved surface. The spray zone axis along the length of the tube remains unchanged. Fig. 4 shows the detailed geometry of the volumetric distribution model. The model developed in this study can be applied to nozzle-to-surface heights that are greater or smaller than the tube radius, despite the fact that the nozzle arrangement in this study requires the latter.

As discussed by Mudawar and Estes [21], the differential area, dA' of a spherical surface of radius H, equal to the distance between the orifice and the tube's surface, is given by

$$dA' = 2\pi H^2 \sin\gamma d\gamma. \tag{1}$$

Based on the point-source depiction of the spray by Mudawar and Estes, a uniform volumetric flux over the spherical surface is defined as

$$Q''_{sp} = \frac{Q}{2\pi H^2[1-\cos(\theta/2)]}. \tag{2}$$

The oval passing through point S on the surface in Fig. 4 has the area

$$A = \pi(H\tan\gamma)\left(\frac{D}{2}\sin\beta\right). \tag{3}$$

The projection of dA' on the tube's surface is another differential area, dA, which can be obtained by differentiating Eq. (3).

$$dA = 2\pi H^2 \sin\gamma\left|\left(\frac{D}{4H}\right)\frac{\cos\beta}{\cos\gamma}\left\{\frac{\tan\beta}{\sin\gamma\cos\gamma}+\frac{d\beta}{d\gamma}\right\}\right|d\gamma. \tag{4}$$

Applying the sine rule to triangle NOS in Fig. 4,

$$\frac{H-D/2}{\sin\{\pi-(\pi-\beta+\gamma)\}} = \frac{D/2}{\sin\gamma}, \tag{5}$$

which yields

$$\beta = \sin^{-1}\left\{\left(\frac{2H}{D}-1\right)\sin\gamma\right\}+\gamma. \tag{6}$$

Differentiating Eq. (6) yields

$$\frac{d\beta}{d\gamma} = \left(\frac{2H}{D}-1\right)\frac{\cos\gamma}{\cos\beta\cos\gamma+\sin\beta\sin\gamma}+1. \tag{7}$$

Combining Eqs. (6) and (7) into Eq. (4) gives

$$dA = 2\pi H^2\frac{\sin\gamma}{\cos^3\gamma}\left[\frac{D}{4H}\left\{\sin\beta\cot\gamma+\cos\beta\cos^2\gamma+\cos^2\gamma\left(\frac{2H}{D}-1\right)\times\frac{1}{1+\tan\beta\tan\gamma}\right\}\right]d\gamma. \tag{8}$$

The spray volumetric flux along the curved impact surface can be obtained by combining Eqs. (1), (2) and (8).

$$Q'' = Q''_{sp}\frac{dA'}{dA} = \frac{Q}{2\pi H^2[1-\cos(\theta/2)]}\cos^3\gamma\left[\frac{D}{4H}\{\sin\beta\cot\gamma+\cos\beta\cos^2\gamma+\cos^2\gamma\left(\frac{2H}{D}-1\right)\frac{1}{1+\tan\beta\tan\gamma}\}\right]^{-1}. \tag{9}$$

Fig. 4 shows that the half-angle of the tube's representative section is related to the spray's cone angle by the relation (obtained using the sine rule)

Table 3
Spray quenching heat transfer correlations.

Boiling regime	Correlation
Single phase [13,24]:	$T_{OSP} = 13.43Re_{32}^{0.167}Pr_f^{0.123}\left(\frac{k_f}{d_{32}}\right)^{0.22}+T_f$
	$Nu_{d_{32}} = 4.7Re_{d_{32}}^{0.61}Pr_f^{0.32}$
Nucleate boiling [24]:	$\frac{q''d_{32}}{\mu_f h_{fg}} = 0.00479\left\{\frac{c_{p,f}(T_s-T_f)}{h_{fg}}\right\}^{5.75}\left(\frac{\rho_f}{\rho_g}\right)^{2.5}\left(\frac{\rho_f\overline{Q}''^2 d_{32}}{\sigma}\right)^{0.35}$
Critical Heat Flux [24]:	$\frac{q''_{m,p}}{\rho_g h_{fg}Q''} = 2.3\left(\frac{\rho_f}{\rho_g}\right)^{0.3}\left(\frac{\rho_f Q''^2 d_{32}}{\sigma}\right)^{-0.35}\left(1+0.0019\frac{\rho_f c_{p,f}\Delta T_{sub}}{\rho_g h_{fg}}\right)$
Transition boiling [15]:	$q'' = q''_{CHF}-\frac{q''_{CHF}-q''_{MIN}}{(\Delta T_{CHF}-\Delta T_{MIN})^3}\left[\Delta T_{CHF}^3-3\Delta T_{CHF}^2\Delta T_{MIN}+6\Delta T_{CHF}\Delta T_{MIN}\Delta T-3(\Delta T_{CHF}+\Delta T_{MIN})\Delta T^2+2\Delta T^3\right]$
Minimum heat flux [15]:	$q''_{MIN} = 3.324\times10^6 Q''^{0.544}U_m^{0.324}$
	$\Delta T_{MIN} = 2.049\times10^2 Q''^{0.066}U_m^{0.138}d_{32}^{-0.035}$
Film wetting [22]:	$q'' = q''_{MIN}+\frac{q''_{DFB}-q''_{MIN}}{(\Delta T_{DFB}-\Delta T_{MIN})^3}\left[(3\Delta T_{DFB}-\Delta T_{MIN})\Delta T_{MIN}^2-6\Delta T_D FB\Delta T_M IN\Delta T+3(\Delta T_D FB+\Delta T_M IN)\Delta T^2-2\Delta T^3\right]$
	$+\left.\frac{\partial q''}{\partial\Delta T}\right\|_{DFB}\frac{1}{(\Delta T_{DFB}-\Delta T_{MIN})^2}\left[-\Delta T_{DFB}\Delta T_{MIN}^2+(2\Delta T_D FB+\Delta T_M IN)\Delta T_M IN\Delta T-(\Delta T_D FB+2\Delta T_M IN)\Delta T_2+\Delta T^3\right]$
	$\left.\frac{\partial q''}{\partial\Delta T}\right\|_{DFB} = 1.164\times10^4 Q''^{0.397}U_m^{0.0995}d_{32}^{-0.0366}$
	$q''_{DFB} = 6.1\times10^6 Q''^{0.589}U_m^{0.244}$
	$\Delta T_{DFB} = 886.2Q''^{0.192}U_m^{0.144}d_{32}^{0.0367}$
Film boiling [15]	$q'' = 63.25\Delta T^{1.691}Q''^{0.264}d_{32}^{-0.062}$

Units: q'' [W m^{-2}], $\Delta T = T_s - T_f$ [°C], Q'' [m^3 s^{-1} m^{-2}], U_m[m s^{-1}], d_{32} [m], h [W m^{-2}K^{-1}], ρ_f[kg m^{-3}], h_{fg} [J kg^{-1}], $c_{p,f}$ [J kg^{-1}K^{-1}], k_f [W m^{-1} K^{-1}], μ_f[N s m^{-2}], σ [N m^{-1}]. $(T_s+T_f)/2$ is used in single-phase regime and saturation temperature in other regimes to evaluate fluid properties.

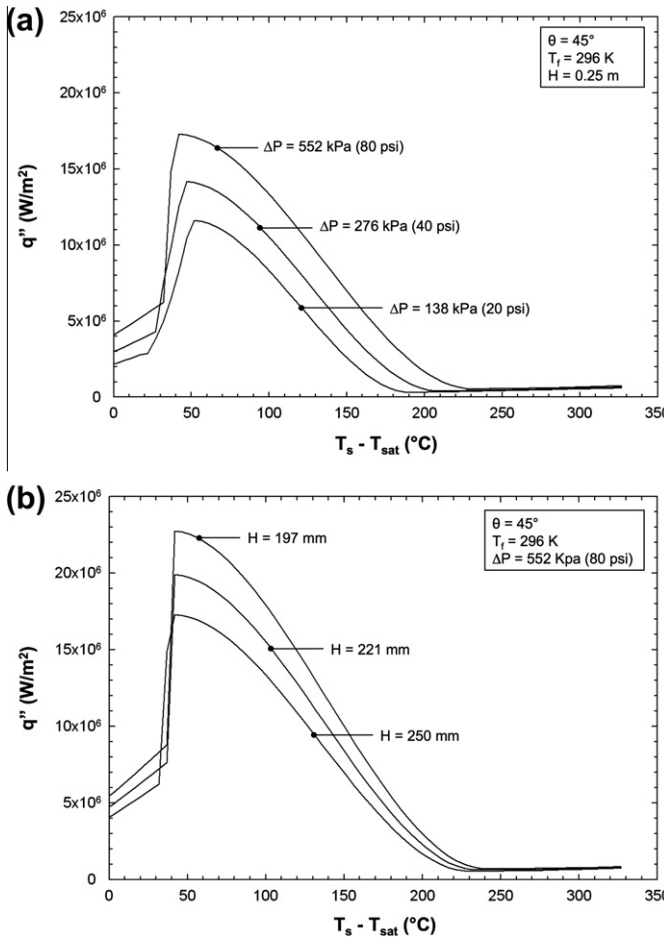

Fig. 7. Variations of spray boiling curve along spray axis with (a) ΔP for $H = 0.25$ m, and (b) H for $\Delta P = 552$ kPa (80 psi).

$$\varphi = \sin^{-1}\left\{\left(\frac{2H}{D} - 1\right)\sin(\theta/2)\right\} + \theta/2 \tag{10}$$

and the outer edge of the spray's impact area is an ellipse whose major and minor diameters are given, respectively, by

$$2a = 2H\tan(\theta/2) \tag{11}$$

$$\text{and} \quad 2b = D\sin\varphi. \tag{12}$$

The mean volumetric flux across an *equivalent flat impact area* (not true curved impact area) is given by

$$\overline{Q}'' = \frac{Q}{\pi ab} = \frac{Q}{\pi\{H\tan(\theta/2)\}\{\frac{D}{2}\sin\varphi\}}. \tag{13}$$

Introducing the relation $r = H\tan\gamma$ (from Fig. 4) and combining Eqs. (9) and (13) give

$$\frac{Q''}{\overline{Q}''} = \left[\frac{\tan(\theta/2)\sin\varphi}{1-\cos(\theta/2)}\right]\frac{1}{\left\{1+\left(\frac{r}{H}\right)^2\right\}^{3/2}} \times\left\{\frac{\sin\beta}{\left(\frac{r}{H}\right)} + \frac{\cos\beta}{1+\left(\frac{r}{H}\right)^2} + \frac{1}{1+\left(\frac{r}{H}\right)^2}\left(\frac{2H}{D}-1\right)\frac{1}{1+\left(\frac{r}{H}\right)\tan\beta}\right\}^{-1}, \tag{14}$$

$$\text{where} \quad \beta = \sin^{-1}\left\{\left(\frac{2H}{D}-1\right)\frac{\left(\frac{r}{H}\right)}{\sqrt{1+\left(\frac{r}{H}\right)^2}}\right\} + \tan^{-1}\left(\frac{r}{H}\right). \tag{15}$$

The spatial volumetric distribution along the curved impact surface of the tube is shown in Figs. 5(a)–(c) and 6 for different spray nozzle conditions. For a given value of nozzle-to-surface distance, H, Q'' decreases very slowly from its maximum value at $r = 0$ to $r = 0.5a$. In this span, the reduction in Q'' is only 2%, compared to 7–8% beyond $r = a$. Figs. 5(a)–(c) show that the peak value of Q'' at $r = 0$ increases with increasing nozzle pressure drop, ΔP, since the total spray flow rate Q also increases with increasing ΔP. Comparing Figs. 5(a) and 6 shows the peak value of Q'' increases with decreasing H, a consequence of increased spray concentration in a smaller area for the smaller H. However, the total spray rate, Q, reaching the surface is unchanged because ΔP is the same for both H values. Also, as the nozzle is brought closer to the surface, Fig. 6, Q'' drops by a greater magnitude between $r = 0$ and $r = a$. It should be noted that two values of H examined here (25 and 19.7 cm) are carefully selected to ensure that the entire inner wall of the tube is impacted by a fixed number of sprays (8 and 10, respectively).

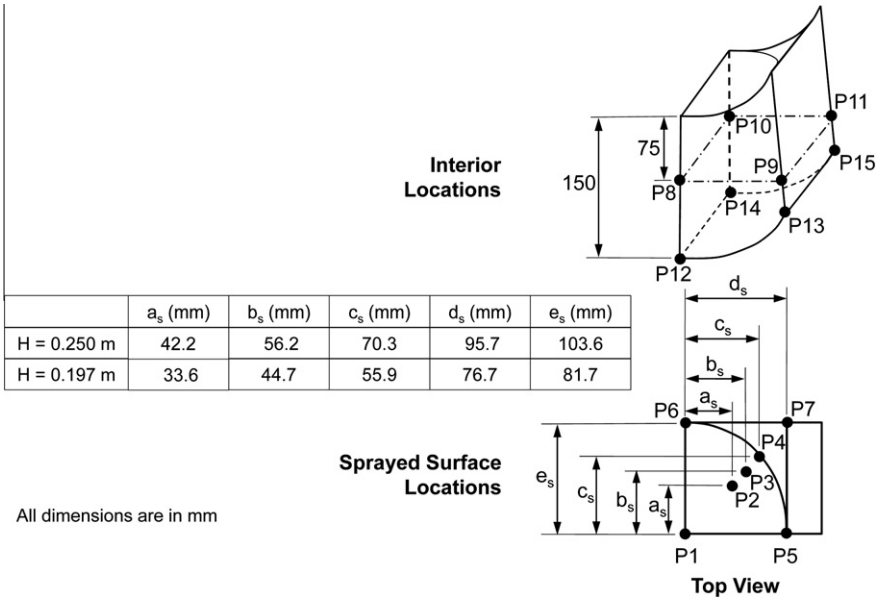

	a_s (mm)	b_s (mm)	c_s (mm)	d_s (mm)	e_s (mm)
H = 0.250 m	42.2	56.2	70.3	95.7	103.6
H = 0.197 m	33.6	44.7	55.9	76.7	81.7

Fig. 8. Locations across sprayed surface and interior of unit cell examined in computational model.

4. Determination of boiling curves for sprayed surface

Another spray parameter important to predicting the spray heat transfer relations corresponding to the different regimes is Sauter mean diameter, d_{32}. This parameter is determined from the nozzle pressure drop, ΔP, and orifice diameter, d_o, based on the following correlation for full cone spray nozzles [20],

$$\frac{d_{32}}{d_o} = 3.67\left[We_{d_0}^{1/2} Re_{d_o}\right]^{-0.259}. \tag{16}$$

The Weber and Reynolds numbers in the above equation are defined as

$$We_{d_o} = \frac{\rho_a (2\Delta P/\rho_f) d_0}{\sigma} \tag{17}$$

$$\text{and} \quad Re_{d_o} = \frac{\rho_f (2\Delta P/\rho_f)^{1/2} d_0}{\mu_f}. \tag{18}$$

Correlations that describe spray heat transfer for the different boiling regimes are available in terms of the spray parameters [7,13,15,22,24] and are given in Table 3. The film wetting regime is accounted for in the form of a cubic expression that ensures a continuous and differentiable boiling curve at this regime's transition points [22]. Notice that when applying the CHF relation given in Table 3, CHF is assumed to occur first along the outer rim of the spray impact area along the major axis, where Q'' is lowest.

The nozzle data from Table 1 are used in Eqs. (14) and (16) to determine Q'' and d_{32}, respectively, which, when inserted into the correlations given in Table 3, yield local transient relations between the spray cooling heat flux and wall temperature for each of the boiling regimes. The mean velocity data required by the correlations are also given in Table 1. The transient relations are used to develop complete boiling curves for the different spray conditions considered in the study.

Fig. 7(a) and (b) show boiling curves that are determined along the spray axis for different values of nozzle pressure drop, ΔP, and orifice-to-surface distance, H, respectively. Shown is a monotonic increase in CHF with increasing ΔP, Fig. 7(a), or decreasing H, Fig. 7(b). Heat transfer rate in the nucleate, transition and single-phase regimes is increased and the transition points between boiling regimes (with the exception of T_{CHF}) shifted to higher temperatures with increasing ΔP and/or decreasing H. These trends can be explained by the increasing volumetric flux with increasing ΔP or decreasing H as shown earlier in Figs. 5(a)–(c) and 6. Notice that, because heat flux in the film boiling, film-wetting, and single-phase liquid cooling regimes is a weak function of Q'', the heat flux changes in response to the changes in ΔP or H are far less significant than those for the other regimes.

5. Determination of quench curves

In this study, the thermal simulation is performed using ANSYS, a finite element analysis tool that is popular in metal processing industries. Because of thermal symmetry, the simulation is simplified by considering a quarter of the representative portion of the

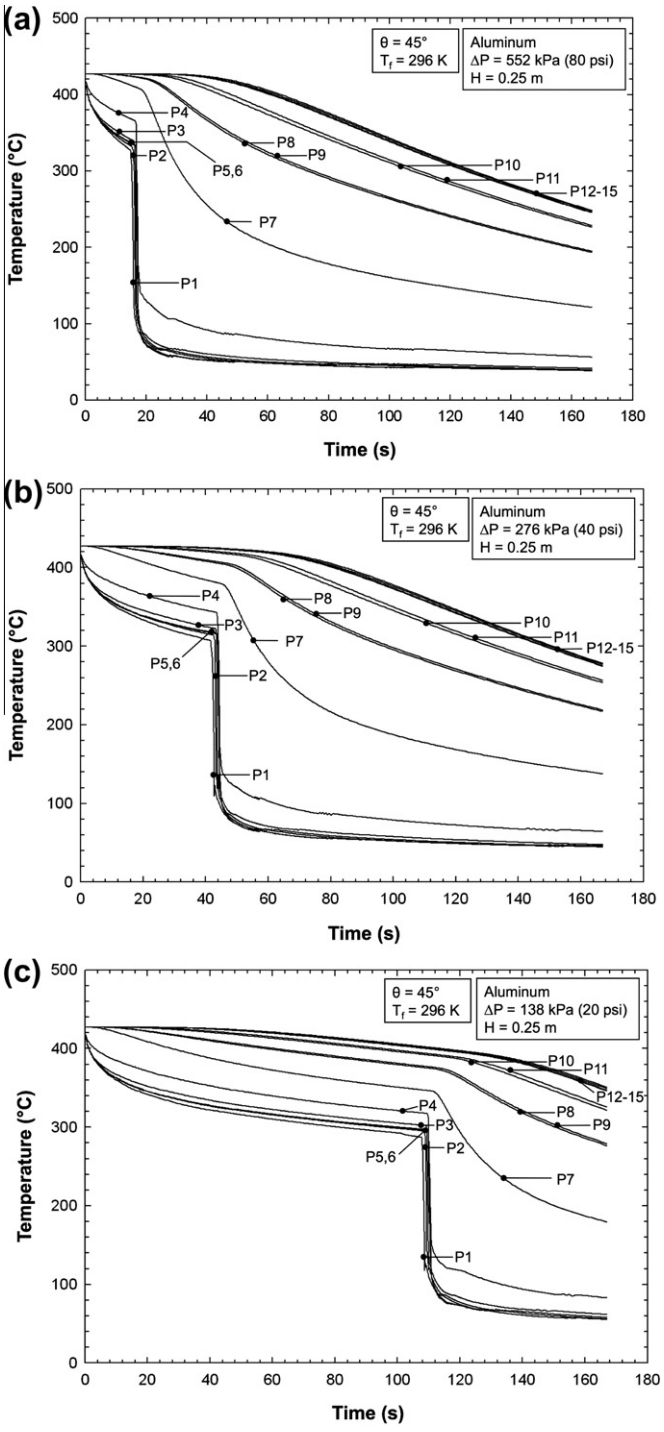

Fig. 9. Spray quench curves for aluminum with $H = 0.25$ m and (a) $\Delta P = 552$ kPa (80 psi), (b) $\Delta P = 276$ kPa (40 psi) and (c) $\Delta P = 138$ kPa (20 psi).

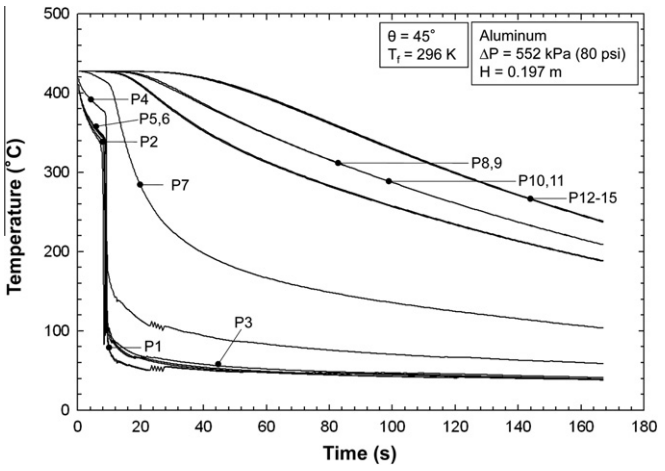

Fig. 10. Spray quench curves for aluminum with $\Delta P = 552$ kPa (80 psi) and $H = 0.197$ m.

tube impacted by a single spray and depicted in Fig. 3. ANSYS analysis is comprised of three stages: pre-processing, solution and post-processing. Pre-processing is the input stage, where all inputs required for analysis are supplied to the software including the model dimensions, material properties and boundary conditions. The boundary conditions in this case are the spray heat flux within the impact area along the inner wall of the unit cell, and perfect insulation on all the other surfaces. Solution stage is the internal computation phase of ANSYS, subject to the constraints set by the user, such as convergence requirements and solution methodology. The simulation has to be able to alter inputs based on changes in the spray cooling boundary as a function of time. This requires a macro written in ANSYS Parametric Design Language (ADPL) to capture nodal temperature data repeatedly at the end of every time step and then use this data to update the spray heat flux on the impact surface. Post-processing is the output stage of ANSYS where the results are provided.

Although steel quenching is typically achieved at very high initial temperatures, the same isothermal initial condition of 427 °C is applied to the unit cell for both aluminum alloy and steel based on typical operating conditions for aluminum alloys, and to facilitate direct assessment of material property effects on the quench curve by comparing results for the two alloys. The analysis is terminated when the surface reaches nearly room temperature (25 °C) and the cooling is felt on the outer surface of the tube.

ANSYS output contains temperatures at all locations in the unit cell as a function of time. Fig. 8 shows locations of interest in the unit cell that reflect the significant spatial variations in cooling behavior that occur during the quench. Selection of these locations is guided in part by the variations in volumetric flux depicted in Figs. 5(a)–(c) and 6. In Fig. 8, *P*1–*P*4 are representative points along the curved surface impacted by the spray that are selected to trace surface cooling variations at and away from the spray axis. Points *P*5–*P*7 in the same curved surface provide additional insight into surface cooling variations at and beyond the outer periphery of the spray impact area. The remaining points *P*8–*P*15 internal to the tube are chosen to track the delayed thermal response to the spray away from the sprayed surface.

Figs. 9(a)–(c) and 10 show quench curves for the aluminum alloy tube, and Figs. 11(a)–(c) and 12 for the steel tube. Shown in these plots are the influences of nozzle pressure drop, ΔP, and office-to surface distance, H, for all the locations indicated in Fig. 8. Notice that the different locations may be grouped into two separate clusters. Cluster 1 includes points *P*1–*P*6 that fall along the curved surface impacted by the spray, while cluster 2 includes points *P*7–*P*15 whose response is delayed by heat diffusion effects. The quench curves for both alloys show a clear distinction in thermal response between the two clusters, with cluster 1 following fairly conventional quench trends and cluster 2 displaying slower, delayed cooling.

Figs. 9(a)–(c) highlight the effects of ΔP on the quench curves for aluminum. Higher ΔP is shown hastening the onset of the rapid cooling stages of the quench. This can be explained by drawing parallels to the boiling curve trends discussed earlier. It can also be seen that the overall transition from the film boiling regime

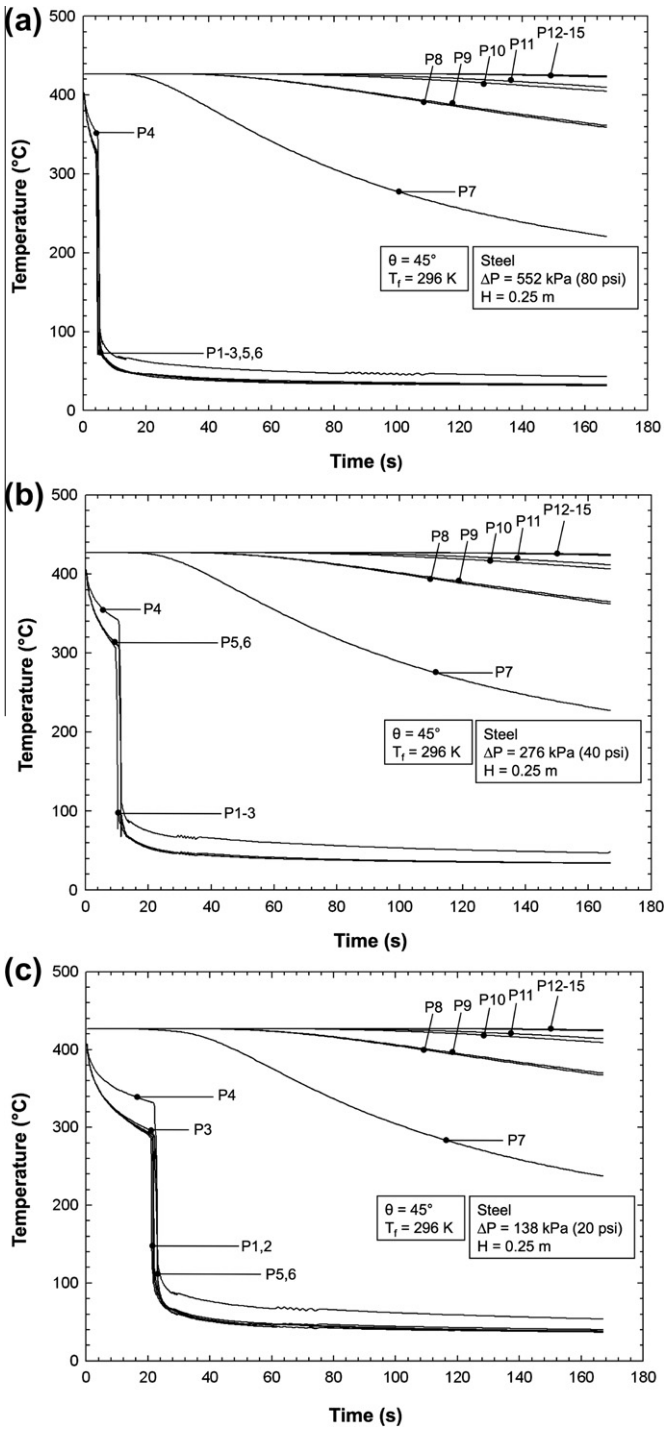

Fig. 11. Spray quench curves for steel with H = 0.25 m and (a) ΔP = 552 kPa (80 psi), (b) ΔP = 276 kPa (40 psi) and (c) ΔP = 138 kPa (20 psi).

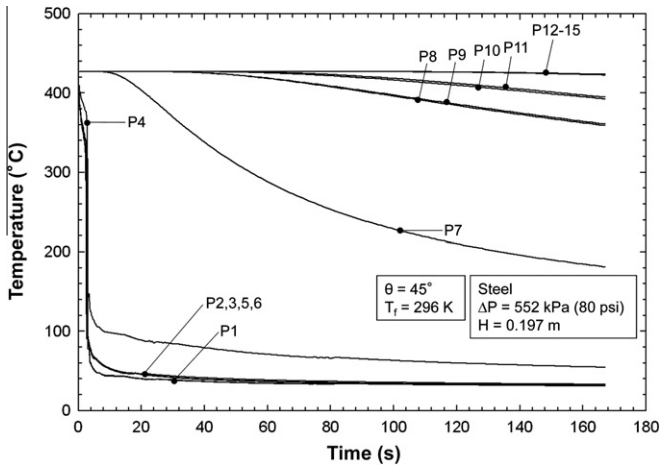

Fig. 12. Spray quench curves for steel with ΔP = 552 kPa (80 psi) and H = 0.197 m.

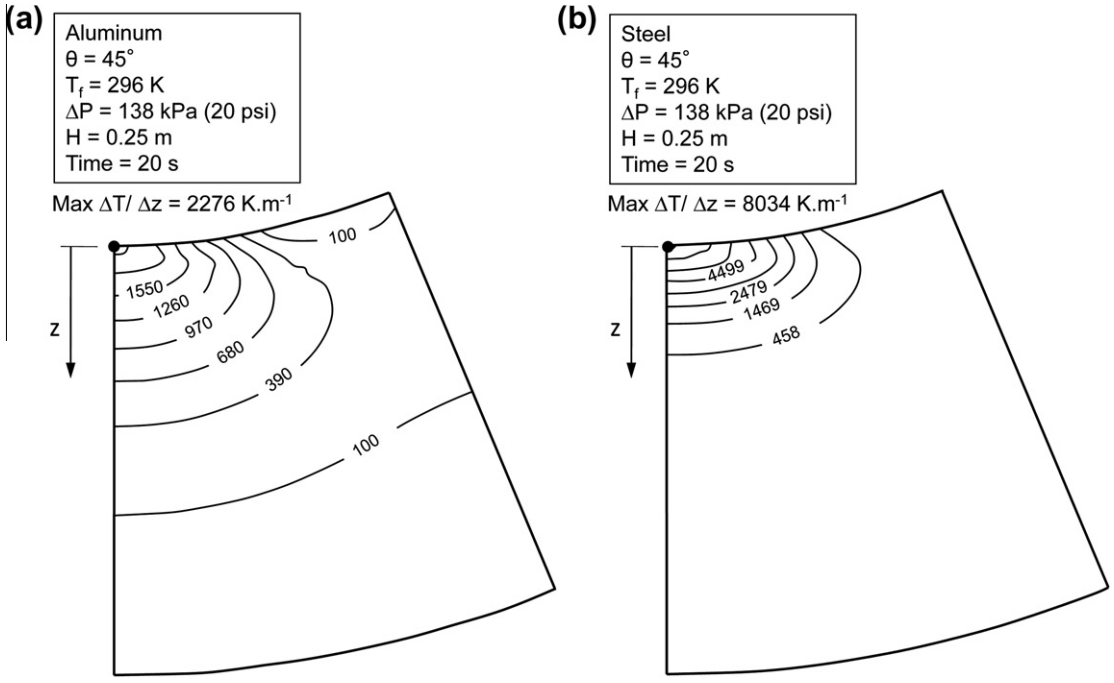

Fig. 13. Temperature gradients in unit cell 20 s into the quench for (a) aluminum and (b) steel.

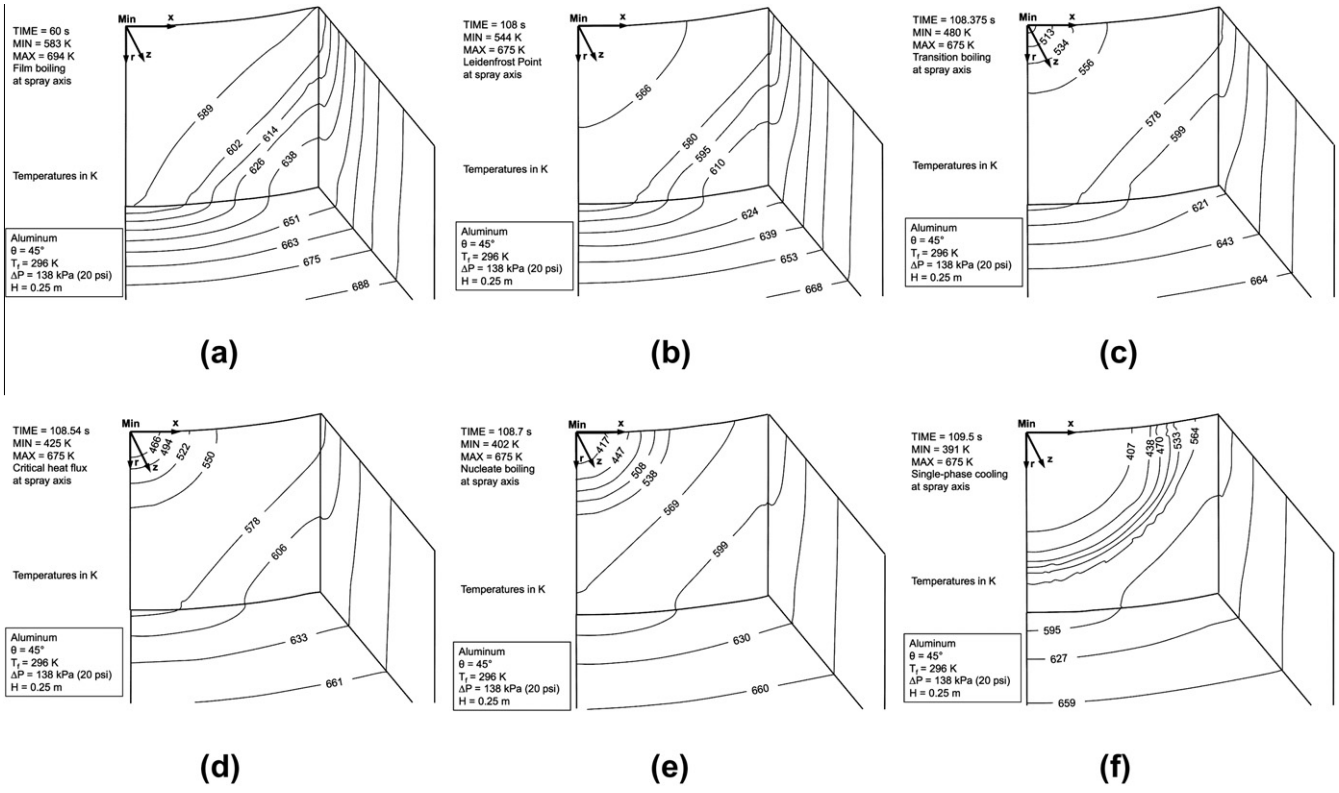

Fig. 14. Temperature contour plots in aluminum unit cell during spray quench with ΔP = 138 kPa (20 psi) and H = 0.25 m corresponding to times when surface at spray axis is (a) in film boiling, (b) at Leidenfrost point, (c) in transition boiling, (d) at critical heat flux point, (e) in nucleate boiling, and (f) in single-phase liquid cooling regime.

to the single-phase regime at any location along the sprayed surface takes place within a very short span of time (~5 s), which highlights the high cooling effectiveness of sprays. Comparing Figs. 9(a) and 10 shows how reducing H has the same overall effect as increasing ΔP.

Figs. 11(a)–(c) and 12 show similar overall trends in the response of the steel tube to variations in ΔP and H. Notice that the entire transition period between the film boiling and single-phase liquid cooling regimes for steel is also quite small (~3 s) for all cases considered.

Comparing the quench curves for aluminum alloy, Figs. 9(a)–(c) and 10, with those for steel, Figs. 11(a)–(c) and 12, points to major differences in the thermal response of the two alloys. For identical ΔP and H values, locations on the surface exposed to the spray (cluster 1) cool much faster for steel than for aluminum. However, locations within the wall (cluster 2) cool a lot slower in steel than in aluminum. These trends can be traced to the large difference in thermal diffusivities of the two alloys, 1.25×10^{-5} m^2/s for steel compared to 8.07×10^{-5} m^2/s for aluminum. With its much greater thermal diffusivity, aluminum facilitates faster penetration of the cooling effect into the wall, rapidly dissipating the surface temperature gradients. This reduces the cooling rate at the aluminum surface, while decreasing temperatures within the wall. Steel, on the other hand, is far slower in conducting the heat away from the surface and into the wall.

These effects are better illustrated in Fig. 13, which shows the thermal gradients developed in the z-direction for the two alloys 20 s into the quench. Notice how the maximum surface temperature gradient for steel is over 3 times greater than for aluminum. Furthermore, the temperature gradient in steel drops to about 5.7% of the maximum surface value within a much shorter distance from the surface compared to the same percentage drop for aluminum.

Fig. 14(a)–(e) show the surface and near-surface temperature contour plots for aluminum for $\otimes P = 138$ kPa (20 psi) and $H = 0.25$ m at particular times during the quench corresponding to different boiling regimes occurring at the intersection of the spray axis and center of the sprayed surface. As discussed earlier, this is also the location where Q'' is highest along the sprayed surface. In the film boiling regime, Fig. 14(a), there is a fairly uniform increase in the temperature contour values between the spray axis and outer edge of the impact area. This behavior persists down to the instant the Leidenfrost point is encountered at the axis, Fig. 14(b). Beyond this time, appreciable localized gradients begin to develop around the axis as the heat flux begins to escalate. These localized gradients persist until the single-phase regime is encountered at the axis, Fig. 14(f), at which point the gradients begin to subside.

It is evident from the results of this study that spray quenching offers controlled cooling rates by adjusting the spray nozzle parameters, a feature absent in bath quenching. By adjusting these parameters, it is possible to advantageously manipulate the Leidenfrost point to enhance overall quench rate. It is also possible to achieve a more uniform and predictable quench behavior by careful configuration of the spray system. The predictive approach presented in this paper facilitates the determination of surface temperature gradients in the quenched part to guard against distortion and stress cracks. Additionally, the spray quench curves obtained in this study can be combined with the alloy's temperature–time-transformation curve (also called the *C*-curve [36]) using the *quench-factor technique* [37] to accurately predict the hardness or strength of the metal alloy part produced [37–40]. A detailed discussion of how the quench curve can be combined with the *C*-curve using the quench-factor technique to determine these properties is provided in [18,19].

6. Conclusions

This study examined the problem of spray quenching thick-walled metal alloy tubes. An analytical model was constructed to determine the shape and size of the spray impact zone along the curved inner wall of the tube, as well as the distribution of volumetric flux across the same zone. A method for determining spray boiling curves at every point within the impact zone is discussed. These boiling curves are used as boundary conditions for the quenched surface in a computational model of a unit cell of the tube for both aluminum alloy and steel. The computational model provides quench curves for every point within the sprayed surface and the tube wall. These quench curves are used to assess the influence of spray nozzle pressure drop, orifice-to-surface distance, and thermal properties of the alloy on temperature response to the quench and the impact of the quench on the mechanical properties of the alloy tube. Key findings from the study are as follows.

1. The spray impact zone along the inner surface of the tube is elliptical in shape. Within the impact zone, volumetric flux is highest at the spray nozzle axis and decreases monotonically towards the impact zone's periphery.
2. Increasing nozzle pressure drop or decreasing orifice-to-surface distance increases the magnitude of volumetric flux, which hastens the onset of the rapid cooling stages of the quench as well as improves overall cooling effectiveness.
3. The sprayed surface is characterized by fairly conventional spray quench curves, while regions within the tube wall show more gradual and delayed thermal response due to heat diffusion effects. The cooling rate is slower for locations farther away from the sprayed surface.
4. Because of superior thermal diffusivity of aluminum alloy compared to steel, the sprayed surface cools much faster for steel than for aluminum. However, locations within the wall cool a lot slower in steel than in aluminum.

References

[1] M. Monde, H. Kusuda, H. Uehara, Critical heat flux during natural convection boiling in rectangular channels submerged in saturated liquid, J. Heat Transfer 104 (1982) 300–303.
[2] I. Mudawar, A.H. Howard, C.O. Gersey, An analytical model for near-saturated pool boiling critical heat flux on vertical surfaces, Int. J. Heat Mass Transfer 40 (1997) 2327–2339.
[3] Y. Katto, S. Yokoya, Critical heat flux of forced convective boiling in uniformly heated vertical tube with special references to very large length-to-diameter ratios, Int. J. Heat Mass Transfer 30 (1987) 2261–2269.
[4] T.C. Willingham, I. Mudawar, Channel height effects on forced-convection boiling and critical heat flux from a linear array of discrete heat sources, Int. J. Heat Mass Transfer 35 (1992) 1865–1880.
[5] I. Mudawar, D.C. Wadsworth, Critical heat flux from a simulated electronic chip to a confined rectangular impinging jet of dielectric liquid, Int. J. Heat Mass Transfer 34 (1991) 1465–1480.
[6] D. Wadsworth, I. Mudawar, Enhancement of single-phase heat transfer and critical heat flux from an ultra-high-flux simulated microelectronic heat source to a rectangular impinging jet of dielectric liquid, J. Heat Transfer 114 (1992) 764–768.
[7] Y. Xuan, Q. Li, Heat transfer enhancement of nanofluids, Int. J. Heat Fluid Flow 21 (2000) 58–64.
[8] J.R. Thome, Enhanced Boiling Heat Transfer, Hemisphere Publishing Corporation, New York, NY, 1990.
[9] H. Honda, H. Takamastu, J.J. Wei, Enhanced boiling of FC-72 on silicon chips with micro-pin-fins and submicron-scale roughness, ASME J. Heat Transfer 124 (2002) 383–389.
[10] S. Ujereh, T. Fisher, I. Mudawar, Effects of carbon nanotube arrays on nucleate pool boiling, Int. J. Heat Mass Transfer 50 (2007) 4023–4038.
[11] A.H. Lefebvre, Atomization and Sprays, Hemisphere Publishing Corporation, New York, 1989.
[12] S. Toda, A study in mist cooling (1st report: investigation of mist cooling), Trans. JSME 38 (1972) 581–588.
[13] I. Mudawar, W.S. Valentine, Determination of the local quench curve for spray-cooled metallic surfaces, J. Heat Treat. 7 (1989) 107–121.
[14] T.A. Deiters, I. Mudawar, Prediction of the temperature-time cooling curves for three-dimensional aluminum products during spray quenching, J. Heat Treat. 8 (1990) 81–91.
[15] W.P. Klinzing, J.C. Rozzi, I. Mudawar, Film and transition boiling correlations for quenching of hot surfaces with water sprays, J. Heat Treat. 9 (1992) 91–103.
[16] D.D. Hall, A Method of Predicting and Optimizing the Thermal History and Resulting Mechanical Properties of Aluminum Alloy Parts Subjected to Spray Quenching, MS Thesis, Mechanical Engineering, Purdue University, West Lafayette, IN, 1993.
[17] G.E. Totten, C.E. Bates, N.A. Clinton, Handbook of Quenchants and Quenching Technology, ASM International, Materials Park, OH, 1993.

[18] D.D. Hall, I. Mudawar, Predicting the impact of quenching on mechanical properties of complex-shaped aluminum alloy parts, J. Heat Transfer 117 (1995) 479–488.
[19] D.D. Hall, I. Mudawar, Experimental and numerical study of quenching complex-shaped metallic alloys with multiple, overlapping sprays, Int. J. Heat Mass Transfer 38 (1995) 1201–1216.
[20] K.A. Estes, I. Mudawar, Correlation of Sauter mean diameter and critical heat flux for spray cooling of small surfaces, Int. J. Heat Mass Transfer 38 (1995) 2985–2996.
[21] I. Mudawar, K.A. Estes, Optimizing and predicting CHF in spray cooling of a square surface, J. Heat Transfer 118 (1996) 672–680.
[22] D.D. Hall, I. Mudawar, R.E. Morgan, S.L. Ehlers, Validation of a systematic approach to modeling spray quenching of aluminum alloy extrusions, composites and continuous castings, J. Mater. Eng. Perform. 6 (1997) 77–92.
[23] R.-H. Chen, L.C. Chow, J.E. Navedo, Effects of spray characteristics on critical heat flux in subcooled water spray cooling, Int. J. Heat Mass Transfer 45 (2002) 4033–4043.
[24] J.R. Rybicki, I. Mudawar, Single-phase and two-phase cooling characteristics of upward-facing and downward-facing sprays, Int. J. Heat Mass Transfer 49 (2006) 5–16.
[25] J.W. Hodgson, R.T. Saterbak, J.E. Sunderland, An experimental investigation of heat transfer from a spray cooled isothermal cylinder, J. Heat Transfer 90 (1968) 457–463.
[26] F.P. Buckingham, A. Haji-Sheikh, Cooling of high-temperature cylindrical surfaces using a water-air spray, J. Heat Transfer 117 (1995) 1018–1027.
[27] L.D. Albright, Cooling short cylinders in air using a water spray, Trans. Am. Inst. Agri. Eng. 19 (1976) 762–765.
[28] T.-B. Chang, Effects of nozzle configuration on a shell-and-tube spray evaporator with liquid catcher, Appl. Therm. Eng. 26 (2006) 814–823.
[29] S.A. Moeykens, W.W. Huebsch, M.B. Pate, Heat transfer of R-134a in single-tube spray evaporation including lubrication effects and enhanced surface results, Trans. ASHRAE 101 (1995) 111–123.
[30] S.A. Moeykens, M.B. Pate, The effects of nozzle height and orifice size on spray evaporation heat transfer performance for a low-finned, triangular-pitch tube bundle with R-134a, Trans. ASHRAE 101 (1995) 420–433.
[31] S.A. Moeykens, J.E. Kelly, M.B. Pate, Spray evaporation heat transfer performance of R-123 in tube bundles, Trans. ASHRAE 102 (1996) 259–272.
[32] I.T. Elperin, Heat transfer of two-phase flow with a bundle of tubes, Inzh.-Fiz. Zh. 4 (1961) 30–35.
[33] E.W. Takahara, Experimental Study of Heat Transfer from a Heated Circular Cylinder in Two-Phase, Water-air Flow, MS Thesis, Air Force Institute of Technology, Wright-Patterson AFB, OH, 1966.
[34] N. Mascarenhas, I. Mudawar, Analytical and computational methodology for modeling spray quenching of solid metal alloy cylinders, Int. J. Heat Mass Transfer 53 (2010) 5871–5883.
[35] H.E. Boyer, T.L. Gall (Eds.), Metals Handbook, American Society for Metals, Materials Park, OH, 1985.
[36] W.L. Fink, L.A. Willey, Quenching of 75S aluminum alloy, Trans. Am. Inst. Mining Metallurg. Eng. 175 (1948) 414–427.
[37] J.W. Evancho, J.T. Staley, Kinetics of precipitation in aluminum alloys during continuous cooling, Metallurg. Trans. 5 (1974) 43–47.
[38] J.T. Staley, Quench factor analysis of aluminum alloys, Mater. Sci. Technol. 3 (1987) 923–935.
[39] J.W. Cahn, Transformation kinetics during continuous cooling, Acta Metallurg. 4 (1956) 572–575.
[40] C.E. Bates, Predicting properties and minimizing residual stress in quenched steel parts, J. Heat Treat. 6 (1988) 27–45.